Source of Acquisition
NASA Goddard Space Flight Center

The *Suzaku* Observation of NGC 3516: Complex Absorption and the Broad and Narrow Fe K Lines

Alex MARKOWITZ[1,2], James N. REEVES[1,2], Giovanni MINIUTTI[3], Peter SERLEMITSOS[1], Hideyo KUNIEDA[4,5], Tahir YAQOOB[2], Andrew C. FABIAN[3], Yasushi FUKAZAWA[6], Richard MUSHOTZKY[1], Takashi OKAJIMA[1], Luigi GALLO[7], Hisamitsu AWAKI[8], Richard E. GRIFFITHS[9]

(Received ; accepted)

Abstract

We present results from a 150 ksec *Suzaku* observation of the Seyfert 1 NGC 3516 in October 2005. The source was in a relatively highly absorbed state. Our best-fit model is consistent with partial covering by a lowly-ionized absorber with a column density near 5×10^{22} cm^{-2} and with a covering fraction 96–100%. Narrow K-shell absorption features due to He- and H-like Fe confirm the presence of a high-ionization absorbing component as well. A broad Fe Kα diskline is required in all fits, even after the complex absorption is taken into account; an additional partial-covering component is an inadequate substitute for the continuum curvature associated with the broad line. The narrow Fe Kα line at 6.4 keV is resolved, yielding a velocity width commensurate with the optical Broad Line Region. The strength of the Compton reflection hump suggests a contribution mainly from the broad Fe line origin. We include in our model soft band emission lines from He- and H-like ions and radiative recombination lines, consistent with photo-ionization, though a small contribution from collisional ionization is possible.

Key words: galaxies: active — X-rays: galaxies — galaxies: individual (NGC 3516)

1. Introduction

In Seyfert AGN, the 6.4 keV Fe Kα emission line has long been known to be an important diagnostic of the material accreting onto supermassive black holes. The associated Compton reflection hump, frequently seen in Seyfert spectra above $\sim$7 keV and peaking near 20–30 keV (Pounds et al. 1990), indicate that Seyferts' Fe lines may have an origin in optically thick material, such as the accretion disk. Observations with *ASCA* indicated that many Fe Kα lines were broad (FWHM velocities up to $\sim$0.3c) and asymmetrically skewed towards

lower energies, implying an origin in the inner accretion disk; the line profile is sculpted by gravitational redshifting and relativistic Doppler effects (e.g., Tanaka et al. 1995, Fabian et al. 2002). However, *XMM-Newton* and *Chandra* observations have been revealing a more complex picture. A narrow Fe K component (FWHM velocities $\sim$5000 km s^{-1} or less) instead appears to be much more common; these lines' widths suggest emission from distant material, such as the outer accretion disk, the optical Broad Line Region or the molecular torus. Spectral observations in which the broad and narrow components are deconvolved are thus a prerequisite for using the Fe K line as a tracer of the geometry of the emitting gas.

At the same time, there is strong evidence from X-ray and UV grating observations for the presence of ionized material in the inner regions of a large fraction of AGN (e.g., Blustin et al. 2005). High-resolution spectroscopy shows the gas is usually outflowing from the nucleus; typical velocities are $\sim$ a few hundred km s^{-1}. Absorption due to a broad range of ionic species is commonly seen; and for many sources, there is evidence for several different photoionized absorbing components, as opposed to a single absorber, along the line of sight. In the Fe K bandpass, some Seyferts show evidence for absorption by H- or He-like Fe, indicating a zone of highly-ionized absorbing material (e.g., NGC 3783, Reeves et al. 2004).

Cold absorbing gas, with line of sight columns in excess of the Galactic value, routinely observed in Seyfert 2 AGN in accordance with unification schemes (Urry, Padovani 1995), have also been reported in some Seyfert 1 AGN. Importantly, variations in column density on timescales from hours to years have been observed in both Seyfert 1 AGN (e.g., Lamer et al. 2003, Puccetti et al. 2004) and Seyfert 2 AGN (Risaliti et al. 2002; Risaliti et al. 2005), suggesting that the absorbing circumnuclear material is not homogeneous in either Seyfert type.

NGC 3516 is a well-studied, nearby (z=0.008836; Keel 1996) Seyfert 1 AGN that can display strong 2–10 keV flux variability on timescales of hours to years (e.g., Markowitz, Edelson 2004). Previous X-ray spectroscopic observations of NGC 3516 e.g., Nandra et al. (1997) using *ASCA*, have indicated the presence of a broad Fe K line, but this source is known to also contain complex and ionized absorption. Numerous UV absorption lines, including N V, C IV and Si IV, were observed with the *International Ultraviolet Explorer* (Ulrich, Boisson 1983); absorption line strengths vary on timescales as short as weeks as the absorber responds to variations in the ionizing flux (e.g., Voit et al. 1987). *Hubble Space Telescope* observations have revealed that this component of absorbing gas (henceforth called the "UV absorber") may consist of several distinct kinematic components (Crenshaw et al. 1998).

X-ray spectra of NGC 3516 can exhibit evidence for large columns ($\gtrsim$10^{22} cm^{-2}) of absorbing gas (e.g., Kolman et al. 1993), though the X-ray absorbers can also display variability on timescales of years (e.g., Mathur et al. 1997). Using *Chandra* gratings data from observations in April 2001 and November 2001, Turner et al. (2005) observed K-shell absorption lines due to H- like Mg, Si and S, and He-like Si, evidence for a highly-ionized absorber, likely with column density $\gtrsim$10^{22} cm^{-2}, outflowing at $\sim$1100 km s^{-1}. Simultaneous with these *Chandra*

observations in 2001 were two *XMM-Newton* observations. Turner et al. (2005) modeled the continuum curvature of the two *XMM-Newton* EPIC spectra by including a partial covering, mildly-ionized absorber; the column density was $\sim 2.5 \times 10^{23}$ cm^{-2}, with a covering fraction of $\sim$50%. However, a direct consequence of including this component in the spectral model was that the formal requirement for the broad Fe line vanished, leading to uncertainty as to whether the broad Fe line really existed in NGC 3516. Spectral fitting using an instrument with a wide bandpass is thus necessary to remove such model degeneracies.

In this paper, we report on an observation of NGC 3516 made with the *Suzaku* observatory in October 2005. The combination of the X-ray Imaging Spectrometer (XIS) CCD and the Hard X-ray Detector (HXD) instruments have yielded a broadband spectrum covering 0.3 to 76 keV, allowing us to deconvolve the various broadband emitting and absorbing components. Furthermore, the exceptional response of the XIS CCD and high signal-to-noise ratio of this observation have allowed us to study narrow emission lines in great detail. §2 gives a brief overview of the *Suzaku* observatory, and describes the observation and data reduction. §3 describes fits to the time-averaged spectrum. Variability analysis is briefly discussed in §4. Flux- and time-resolved spectral fits are discussed in §5. The results are discussed in §6, and a brief summary is given in §7.

2. Observations and data reduction

The nucleus of NGC 3516 was observed by *Suzaku* from 2005 October 12 at 13:45 UT until October 15 at 09:07 UT. *Suzaku* was launched 2005 July 10 into a low-Earth orbit. It has four X-ray telescopes (XRTs; Serlemitsos et al. 2007), each with a spatial resolution of 2′ (HPD). The XRTs focus X-rays onto four X-ray Imaging Spectrometer (XIS; Koyama et al. 2007) CCDs, which are sensitive to 0.2–12 keV X-rays on a 18′ by 18′ field of view, contain 1024 by 1024 pixel rows each, and feature an energy resolution of $\sim$150 eV at 6 keV. Three CCDs (XIS0, 2 and 3) are front-illuminated (FI), the fourth (XIS1) is back-illuminated (BI) and features an enhanced soft X-ray response. The XRT/XIS combination yields effective areas per detector of roughly 330 cm^2 (FI) or 370 cm^2 (BI) at 1.5 keV, and 160 cm^2 (FI) or 110 cm^2 (BI) at 8 keV. Each XIS is equipped with two ^{55}Fe calibration sources which produce fluorescent Mn Kα and Kβ lines and are located at the CCD corners. *Suzaku* also features a non-imaging, collimated Hard X-ray Detector (HXD; Takahashi et al. 2007); its two detectors, PIN and GSO, combine to yield sensitivity from $\sim$10 to $\sim$700 keV. Further details of the *Suzaku* observatory are given in Mitsuda et al. (2007).

2.1. XIS Reduction

The XIS data used in this paper were version 1.2 of the screened data (Fujimoto et al. 2007) provided by the Suzaku team. The screening is based on the following criteria: grade 0, 2, 3, 4, and 6 events were used, the CLEANSIS script was used to remove hot or flickering

pixels, data collected within 256 s of passage through the South Atlantic Anomaly (SAA) were discarded, and data were selected to be 5° in elevation above the Earth rim (20° above the day-Earth rim). The XIS-FI CCDs were in 3x3 and 5x5 editmodes, for a net exposure time after screening of 135.0 (XIS0), 134.8 (XIS2) and 135.2 (XIS3) ks. XIS1 was also in 3x3 and 5x5 editmodes, for a net exposure of 135.4 ks. The XIS was in normal clocking mode.

The source was observed at the nominal center position of the XIS. For each XIS, we extracted a 3′ radius centered on the source. The background was extracted using four circles of radius 1.5′, each located ∼6′ from the source, but chosen to avoid the z=2.1 QSO RX J110741.4+723235, located 4.5′ SE of NGC 3516. Spectra were binned to a minimum of 50 counts bin^{-1} to allow use of the χ^2 statistic.

Response matrices and ancillary response files (ARFs) were generated for each XIS independently using XISSIMRMFGEN and XISSIMARFGEN version 2006-10-26 (Ishisaki et al. 2007). The ARF generator takes into account the level of hydrocarbon contamination on the optical blocking filter. We estimate a carbon column density of 0.8, 1.2, 1.7, and 2.8 $\times 10^{18}$ cm^{-2} for XIS0, 1, 2 and 3, respectively. Finally, we co-added the three XIS-FI spectra using MATHPHA, and co-added the response files and ARFs using ADDRMF and ADDARF, respectively.

To examine the accuracy of the XIS RMFs and determine residual line width due e.g., to imperfect CTI correction, we generated spectra for the ^{55}Fe calibration source lines on each XIS using the above response matrices and ARFs. We fit the calibration source spectra with three Gaussians. Two Gaussians were for the Mn Kα doublet (expected energies 5.899 keV and 5.888 keV), with energy centroids fixed to be 11 eV apart, and the higher energy line flux set to twice that of the lower energy one. The third Gaussian was used to model the Kβ line, expected at 6.490 keV. We found the average of all the calibration line widths σ to be < 4 eV. The Mn Kα line energy centroids for the co-added FI spectrum were consistent with the expected energies to within 1 eV. For XIS1, the Mn Kα line energy centroids were 3±2 eV lower than expected. Such discrepancies are well within the accuracy (∼0.2% at Mn-Kα) of the energy calibration of XIS. Fitting the calibration source lines without the response file, we determined the FWHM energy resolution during the observation to be 145 eV (average of the 4 XISes).

2.2. HXD Reduction

We used data from the HXD-PIN only; NGC 3516 was extremely faint in the HXD-GSO band, and some aspects of the GSO background are still being studied, so we defer analysis of the GSO data to a later time. The PIN source spectra were extracted from cleaned version 1.2 (pre-1.2-r1) HXD event files provided by the HXD instrument team. PIN background count rates are variable and strongly depend on the time since SAA passage (Kokubun et al. 2007), so we selected data according to the following criteria: at least 500 s since SAA passage, COR ≥ 8 GV, and day- and night-Earth elevation angles each $\geq 5°$. Instrumental (non-X-ray) background

spectra for the PIN were provided by the HXD Team ("Background A" model) generated from a time-dependent model. The model utilized the count rate of upper discriminators as the measure of cosmic ray flux that passed through the silicon PIN diode and yielded background spectra based on a database of non X-ray background observations with the PIN (Fukazawa et al. 2007). The current accuracy of the PIN NXB model for a 1 day observation is about 5 % (peak-to-peak residuals). Both the source and background spectra were generated with identical good time intervals, and the source exposure was corrected for instrument dead time (a ~5% effect). This yielded a good time exposure of 105.8 ks.

Data < 12 keV were discarded due to noise contamination near the lower threshold of the PIN diode. Data above 76 keV were also discarded: the gain above an internal Bi Kα calibration line at 76 keV is not well-defined, though the photon statistics above this energy were poor anyway for this observation. Further details of the HXD in-orbit performance are given in Kokubun et al. (2007). To model the contribution to the total background from the Cosmic X-ray Background (CXB), a spectrum of the form $9.0\times10^{-9}(E/3keV)^{-0.29}$ exp(–E/40keV) erg cm^{-2} s^{-1} sr^{-1} keV^{-1} (Gruber et al. 1999) was used. We note that some recent works (e.g., Frontera et al. 2007) suggest a 10% normalization increase compared to Gruber et al. (1999). However, the effect on the net spectrum was negligible; for instance, the change in Compton reflection component strength was 1%, typically. To simulate a CXB spectrum using XSPEC, we assumed a model of the form POWERLAW*HIGHECUT, with photon index Γ=1.29, and low- and high-energy cutoffs of 0.1 and 40 keV, respectively. The power-law normalization of 8.8×10^{-4} ph cm^{-2} s^{-1} keV^{-1} (at 1 keV) was used, appropriate for a source observed in XIS-nominal mode. The 12–76 keV CXB flux was 1.4×10^{-11} erg cm^{-2} s^{-1} (using the Gruber et al. 1999 normalization). The total (X-ray plus particle) background 12–76 keV flux was 4.4×10^{-10} erg cm^{-2} s^{-1}.

The spectrum was binned to a minimum of 400 count bin^{-1}. We used the response file ae_hxd_pinxinom_20060814.rsp. The mean 12–76 keV net source flux and count rate were 1.1×10^{-10} erg cm^{-2} s^{-1} and 0.16 ct s^{-1}. Figure 1 shows the net source, background, and total (source + background) spectra. The source spectrum is always at least 15% of the total up to ~40 keV.

3. Model Fits to the Time-Averaged Spectrum

We used 0.4–1.5 keV data in the XIS-FI spectrum and 0.3–10.0 keV data in the XIS-BI spectrum. We ignored 1.72–1.87 keV in the co-added FI spectrum and 1.80–1.87 keV in the BI spectrum due to uncertainties in calibration associated with the instrumental Si K edge. In all fits, we included a constant to account for relative instrument normalizations. We left the relative XIS-BI/XIS-FI normalization free, but best-fit values were always extremely close to 1.00. The PIN/XIS-FI normalization was kept fixed at 1.13, a value derived using *Suzaku* observations of the Crab (Yamasaki et al., in prep.). All errors on one interesting parameter

correspond to $\Delta\chi^2 = 2.71$ (with the XIS-BI/XIS-FI normalization left free). A redshift of z=0.008836 was used throughout. The abundances of Lodders (2003) were used. A neutral Galactic column of 2.94×10^{20} cm^{-2} was included (Dickey, Lockman 1990).

3.1. Preliminary Broadband Fits

The X-ray continuum emission of Seyfert 1 AGN is usually dominated by a power-law component thought to originate from inverse Comptonization of soft seed photons by a hot corona near the central black hole (e.g., Shapiro et al. 1976; Sunyaev, Titarchuk 1980; Haardt et al. 1994). A simple power-law (henceforth denoted the "primary power-law") over 0.3–76 keV yielded a very poor fit, with χ^2/dof (degrees of freedom) = 49708/1449. As shown in Figure 2(a), residuals strongly indicated the need to include absorption to account for continuum curvature $\lesssim$3 keV. The narrow 6.4 keV Fe Kα line was also obvious.

We therefore added an absorbing column to the power-law, assuming a covering fraction of 1 and systemic redshift (this component is henceforth denoted the "primary absorber"). We used the XSTAR table *grid25BIG_mt.fits*. We also added Gaussians to model Fe Kα and Kβ emission lines. The Fe Kβ energy centroid was kept fixed at 7.06 keV; the normalization was kept fixed at 0.13 times that of the Kα line. With these changes to the model, χ^2/dof fell to 8311.962/1444. The best-fit ionization parameter and column density were $\log(\xi) = 2.0\pm0.1$ erg cm s^{-1} and $7.1\pm0.2\times10^{22}$ cm^{-2}, respectively ($\xi \equiv 4\pi F_{\rm ion}/n$; $F_{\rm ion}$ is the 0.5–20 keV ionizing continuum flux; n is the density of the reflecting material). However, as shown in Figure 2(b), this model did not accurately describe the broadband emission.

To attempt to model the soft emission, we added a second power-law (the "soft power-law"), with photon index Γ tied to the primary power-law; χ^2/dof fell to 3038.86/1443. As shown in Figure 2(c), residuals suggested the presence of soft X-ray emission lines, e.g., near 0.56 keV, likely due to O VII.

We added 13 Gaussians to our model, widths σ were fixed at 0.5 eV. Energy centroids for the lower signal-to-noise ratio lines were kept fixed at lab-frame energies. Table 1 shows the results for the lines in our best-fit baseline model (see below). Data/model residuals for these emission lines are shown in Figure 3. It was significant at $\geq$ 99.0% confidence in an F-test to include each line in the fit. We identify these lines as originating in H-like C, N, O, Ne and Mg, and He-like N, O, Ne and Mg. We also report radiative recombination (RRC) lines of O VII, O VIII and Ne IX (and possibly C VI, blended with the 0.500 keV N VII emission line). The lines are likely attributed to photo-ionization. Most of these lines have been reported previously; we refer the reader to Turner et al. (2003) for results using the *XMM-Newton*-RGS. The strongest line detected in both the RGS spectrum and the *Suzaku* spectrum is O VII. We also included a line near 0.83 keV for Fe L XVII, to model any contribution from collisionally-ionized gas. Turner et al. (2003) included a Mg XI recombination edge component; we eschew it in favor of a Mg XII line at 1.47 keV. Including these emission lines in the model resulted

in χ^2/dof falling to 2346.72/1424. Figure 2(d) shows the residuals to the data after the soft X-ray lines are modeled.

Residuals in the PIN band, peaking near 20–30 keV, signaled the need to include a Compton reflection component. We added a PEXRAV component, assuming solar abundances, a cut-off energy fixed at 400 keV, an inclination fixed at 30°, and a normalization tied to that of the primary power-law. Initially, we assumed that the reflector is subject to the same absorption as the primary power-law. In the best fit-model, χ^2/dof fell to 1895.49/1423, and the value of the reflection fraction R (defined as $\Omega/2\pi$, where Ω is the solid angle subtended by the reflector) was $2.8^{+0.4}_{-0.2}$. The photon index Γ was $2.142^{+0.020}_{-0.007}$. As shown in Figure 2(e), the residuals in the PIN band were thus corrected.

The uncertainty on the relative PIN/XIS cross-normalization is about 1%; the subsequent effect on R is smaller than that associated with the uncertainty of the PIN NXB. We modified the intensity of the PIN NXB by ±2%, which is the 1σ level of the current reproducibility of the PIN NXB. R changed by ±0.2, which is smaller than the statistical error on R. Errors quoted on R for the remainder of this paper are the statistical errors only; readers should bear in mind the additional systematic uncertainty associated with the NXB.

Finally, we re-fit the model, assuming that the PEXRAV component was not affected by the primary absorber. This yielded a goodness of fit nearly identical to the previous fit, with $\chi^2/dof = 1479.3/1417$. All fit parameters were virtually identical to the previous fit; for instance, R was 1.9±0.4.

There remained residuals in the 5–6 keV band. We first discuss modeling these residuals using relativistic diskline components, and later (§3.2) we will discuss if a partial covering component could provide as good a fit. We added two LAOR components (Laor 1991) for relativistic Fe Kα and Fe Kβ emission. Formally, the Kβ diskline is not required (omission of this component does not change χ^2/dof significantly), but we include it for completeness. The normalization of the Kβ diskline was fixed at 0.13 times that of the Kα diskline. The Fe Kα line energy was constrained to lie within rest-frame energies of 6.40 and 6.96 keV; the Kβ line energy was fixed at 7.06 keV. All other parameters were kept tied between the Kα and Kβ components. The emissivity index β (used when quantifying the radial emissivity per unit area as a power-law, $r^{-\beta}$) was fixed at 3.0. Initially, the disk inclination i was fixed at 30°. The outer radius $R_{\rm out}$ was kept fixed at 400 $R_{\rm g}$ (1 $R_{\rm g} \equiv GM_{\rm BH}/c^2$). The inner radius $R_{\rm in}$ was left free but set at 2 $R_{\rm g}$ initially. With the best-fit model, χ^2/dof fell to 1642.51/1420, and the data/model residuals near 5–6 keV were improved considerably; see Figure 2(f). It was significant at >99.99% confidence in an F-test to thaw i; in this and all subsequent models, we set the inclination of the PEXRAV component to that of the diskline. χ^2/dof fell to 1521.46/1419 for $i < 23°$. We refer to this model as the "1-absorber + Compton reflection + diskline" model. Other model parameters are listed in Table 2.

Visual inspection of the data/model residuals in the Fe K bandpass suggested some dips

near 6.7 and 6.9 keV, at the rest-frame energies for Fe XXV and Fe XXVI; see Figure 4(a). Such absorption features might be expected, given the detection of a high-ionization absorber by Turner et al. (2005). Adding a narrow (σ = 0.5 eV) Gaussian with energy centroid fixed at 6.70 keV yielded an improvement in fit of $\Delta\chi^2$=–6.3 (for one less dof), significant at 98.4% in an F-test. The absolute values of the intensity and equivalent width EW were 4±2 $\times 10^{-6}$ ph cm^{-2} s^{-1} and 9±4 eV. Adding a Gaussian at 6.96 keV, χ^2 fell by 7.9, significant at 99.4% in an F-test. The absolute values of the intensity and equivalent width EW were 3±2 $\times 10^{-6}$ ph cm^{-2} s^{-1} and 9±5 eV.

The *Chandra*-HETGS spectrum yielded narrow absorption features ~1–3 keV due to highly-ionized Mg, Si, and S, but we do not significantly detect any narrow absorption features at those energies. A small dip in the spectrum near 2.3 keV is close to the expected energy for S XII. However, XSTAR models demonstrate that S XV absorption, though not significantly detected here, is always stronger than S XII. This feature is more likely due to calibration uncertainty associated with an instrumental Au M edge.

To model these absorption features, we added a second XSTAR component (henceforth denoted the "high-ionization absorber"). Based on the results of Turner et al. (2005), we assumed an outflow velocity of 1100 km s^{-1}. χ^2/dof fell to 1485.04/1417. In this model, the high-ionization absorber had a column $4.0^{+4.6}_{-3.1} \times 10^{22}$ cm^{-2}, similar to the value used by Turner et al. (2005), and $\log(\xi) = 3.7^{+0.3}_{-0.7}$ erg cm s^{-1}. We henceforth refer to this model as our "2-absorber" or "baseline" model. Data/model residuals are shown in Figures 2(g) and 4(b). The primary power-law, with $\Gamma = 1.91^{+0.04}_{-0.05}$, was absorbed by a column 5.5±0.2 $\times 10^{22}$ cm^{-2} and $\log(\xi)$=0.3±0.1 erg cm s^{-1}. Forcing the ionization parameter to a much lower value (e.g., $\log(\xi) \sim -0.5$) resulted in a significantly worse fit, with large residuals at 1.5–3.0 keV; this is likely because the lower ionization does not account for absorption edges due to higher ionization species of Si and S. We caution, however, that this result could be influenced by residual calibration effects in the XIS near 1.8 keV and 2.3 keV (instrumental Si K and Au M edges, respectively). Thawing the diskline emissivity index β yielded no improvement to the fit. We found β was 3.2±2.9; we leave β fixed at 3.0 in subsequent fits. Figure 4(c) shows the data/model residuals when all narrow and broad lines are removed from the fit. Figure 4(d) shows the residuals to the best-fit baseline model when the diskline components are removed and the model re-fit; large residuals and a significantly higher value of χ/dof (1650.66/1421) compared to the baseline model indicated that removing the disklines yielded a significantly worse fit (>99.999% in an F-test). In this model, the strength of the Compton reflection hump was $R = 1.7^{+0.4}_{-0.5}$; a contour plot of R as a function of Γ is shown in Figure 5. Also shown in Figure 5 is a contour plot of R as a function of the PIN/XIS-FI normalization, which had been kept fixed at 1.13; in this plot, Γ was a free parameter. Figure 6 shows an unfolded model spectrum. Other model parameters are listed in Table 2 (see Table 1 for the soft X-ray emission lines).

3.2. *Additional partial covering components*

We next explored the possibility of an additional, partial covering component. Starting with the baseline model, we added a partial covering component consisting of a power-law (with photon index tied to that of the primary power-law) absorbed by an XSTAR component. We first kept the column density $N_{\rm H,PC}$ and ionization parameter $\log(\xi_{\rm PC})$ tied to those of the primary absorber. In the best-fit model (henceforth denoted Model PC1), the added power-law had a normalization 0.32±0.03 times that of the primary power-law. As shown in Table 3, $N_{\rm H}$ and $\log(\xi)$ of the primary absorber and the diskline parameters were consistent with values of the baseline model. However, χ^2/dof was 1485.69/1416, virtually identical to the baseline model, and so there is no formal requirement to include the new partial covering component when the column density and ionization states are tied to those for the primary absorber.

Next, we untied $N_{\rm H,PC}$ and $\log(\xi_{\rm PC})$ and refit (denoted Model PC2). The best-fit parameter values are listed in Table 3. Compared to Model PC1, χ^2 dropped by only 5.2 for 2 additional degrees of freedom, significant at only ∼90% in an F-test. It is thus not highly significant to include the new partial covering component in this case either.

Next, we addressed whether it was possible for a partial covering component to mimic the curvature in the ∼4–6 keV continuum modeled above as a relativistically-broadened Fe line. Starting with the baseline model, we removed the disklines, and added a partial covering component consisting of a power-law (with photon index tied to that of the primary power-law) absorbed by an XSTAR component with a relatively low value of the ionization parameter. The column density needed to be $\gtrsim 10^{22}$ cm^{-2} in order to have a cutoff near ∼4–6 keV. In the best-fit model, the partial coverer had a column of $7.8^{+68}_{-3.8}$[1] × 10^{22} cm^{-2}, and $\log(\xi) = -0.4$ (errors pegged at both hard limits). The new partially-covered power-law had a normalization <0.22 times that of the primary power-law. However, χ^2/dof was 1676.57/1418, a much worse fit compared to the baseline model, and there were still large data/model residuals in the Fe K bandpass; see Figure 2(h). We conclude that a partial coverer cannot mimic the observed curvature of the diskline.

3.3. *Relativistic reflection fits*

Since the broad diskline is a signature of Compton reflection off a possibly-ionized disk, the ionized reflection models of Ross, Fabian (2005) can be used to model the entire reflection spectrum (broad Fe line plus reflection continuum) in a self-consistent manner. We removed the diskline and PEXRAV components from the baseline model, and instead used the grid of models of Ross, Fabian (2005); the ionization parameter ξ was a free parameter but the photon index of the illuminating continuum was tied to that of the primary power-law. The entire reflection spectrum was then convolved with a relativistic LAOR profile; free parameters here were the emissivity index β, inner disk radius $R_{\rm in}$ and disk inclination i. We also included a

[1] parameter error pegged at lower limit

second, unblurred PEXRAV component to model any Compton reflection associated with the narrow 6.4 keV line.

However, due to the heavy absorption present in NGC 3516, any putative soft X-ray excess resulting from blurred and ionized reflection would not be observed. The best-fit model, which had χ^2/dof = list chi-squared suggested a fairly neutral or lowly-ionized reflector, with $\log(\xi) < 1.8$ erg cm s^{-1}. Parameters for the blurring disk were similar to what was obtained in the baseline model: an inclination of 25±10°, an inner disk radius < 4 R_g, and an emissivity index of 3.0±0.5. The total Compton reflection strength R was 2.0 list uncertainty on R, with 2/3 of that associated with the disk reflection, and 1/3 with the narrow Fe line.

3.4. Narrow Fe K line properties

In our baseline model, the best-fit energy centroid for the narrow Fe Kα line was 6.398±0.004 keV, consistent with neutral Fe. The observed line width $\sigma_{\rm obs}$ was 26^{+11}_{-13} eV. The intrinsic line width $\sigma_{\rm intr}$ was found by subtracting in quadrature the ^{55}Fe calibration line width σ of <4 eV from the measured line width. We inferred $\sigma_{\rm intr} = 26^{+11}_{-14}$ eV, which corresponds to a FWHM velocity width of 2800^{+1200}_{-1500} km s^{-1}. This width is consistent with the results obtained by *Chandra*-HETGS for the two observations in 2001, 1290^{+1620}_{-1290} and 3630^{+2350}_{-1540} km s^{-1} (Yaqoob, Padmanabhan 2004).

Figure 7 shows a contour plot of the broad line intensity versus the narrow line intensity, illustrating that the two lines are detected independently at $>4\sigma$ confidence. Such a result is a product of the combination of the narrow response of the XIS (yielding extremely high signal/noise in the narrow line) and *Suzaku*'s broad bandpass. Similar results have been reported e.g., for the *Suzaku* observation of NGC 2992 (Yaqoob et al. 2007).

Finally, we discuss limits to a Fe Kα Compton shoulder. We added a Gaussian emission line at 6.24 keV (rest-frame), with width tied to that of the Kα core. We found an upper limit to the intensity of 7×10^{-6} ph cm^{-2} s^{-1}, or 13% of the Kα core intensity. This limit corresponds to an *EW* of 21 eV.

4. Timing analysis

To compare the variability properties of the primary and soft power-laws, we extracted light curves, summed over all four XISes, orbitally-binned, and background-subtracted, for the 0.3–1.0 and 2–10 keV bands. These light curves are plotted in Figure 8, along with the 12—76 keV orbitally-binned and background-subtracted PIN light curve. For each light curve, we calculated the fractional variability amplitude $F_{\rm var}$ (which quantifies the variability in excess of measurement noise) and its uncertainty following Vaughan et al. (2003). For the 2–10 keV band, $F_{\rm var}$ was $9.3 \pm 0.2\%$, with a maximum/minimum flux ratio of roughly 1.4. $F_{\rm var}$ for the 0.3–1.0 keV was $1.3 \pm 1.8\%$. For the 12–76 keV band, no significant variability in excess of that

due to measurement errors was detected ($F_{\rm var}$ undefined[2]). We note that the systematic error associated with the non-X-ray background for a 5760 s bin was roughly 6 % for the 15–40 keV band (Mizuno et al. 2006).

5. Flux-resolved spectral fits

We performed flux-resolved spectral fits to search for any physical connection between the soft and primary power-laws. Despite the limited flux range exhibited during this observation, we attempted to determine, e.g., if the observed X-ray flux variability could be due to rapid variations in column density of the primary absorber, if both power-laws vary together, or if one power-law is constant. We split the time-averaged spectrum into periods when the 2–10 keV flux was higher and lower than the average 2–10 keV flux of 2.31 $\times 10^{-11}$ erg cm^{-2} s^{-1}, as illustrated in Figure 8. Net exposure times for the high and low-flux spectra for each XIS (and the PIN) were approximately 62.1 (46.3) and 71.3 (59.5) ks, respectively. The average 2–10 keV fluxes were 2.47 and 2.16 $\times 10^{-11}$ erg cm^{-2} s^{-1}, respectively. We applied the best-fitting baseline model from the time-average spectrum to both spectra. All narrow Gaussian energy centroids and widths, β, i and $R_{\rm in}$ for the disklines, and log(ξ) for the high-ionization absorber were kept fixed at their time-averaged values. However, all freed parameters were consistent at the 90% confidence level. For instance, we find no strong evidence that the column density of the high-ionization absorber varies on short timescales. A broadband observation of NGC 3516 spanning a larger flux range is thus needed to potentially distinguish determine if the two power-laws vary in concert.

6. The Search for red and blue-shifted narrow lines

We searched for additional narrow absorption or emission features in the Fe K bandpass, as seen so far in several Seyferts, including NGC 3516. For instance, Turner et al. (2002) found emission lines near 5.57, 6.22, 6.41, 6.53 and 6.9 keV in the November 2001 *Chandra*-HETGS and *XMM-Newton* EPIC spectra of NGC 3516. One interpretation was that they were red- and blue-shifted Fe K lines associated with transient "hot spot" emission on the inner accretion disk.

We searched for such features by adding a Gaussian component to the time-averaged spectrum, with width fixed at 0.5 eV, sliding it over 4–9 keV in energy. In addition to the aforementioned absorption lines at 6.70 and 6.96 keV, there was only one "candidate" feature with $\Delta\chi^2 < -5.0$, an absorption line near 6.0 keV. However, we performed Monte Carlo simulations to assess the statistical significance of this feature (see §3.3 of Porquet et al. 2004 and §4.3.3 of Markowitz et al. 2006 for a description of these simulations), and we found that the line was consistent with photon noise. Furthermore, the feature was evident only in one XIS

[2] Indicates that the measured variance is smaller than that expected solely from measurement noise

camera, and thus is likely not real.

As an aside, we note that a 7.47 keV Ni Kα emission line was not detected in the time-average spectrum; adding a Gaussian at this energy, we found an upper limit of 3 eV.

We also extracted time-resolved spectral slices by dividing the time-averaged spectrum into five slices 48 ks in duration, with each slice having an exposure time near 27 ks per XIS and 21 ks for the PIN. We did not investigate longer time slices since they might miss short-lived hot-spot emission lines; shorter time slices would have yielded poorer photon statistics. Applying a sliding narrow Gaussian over 4–9 keV in each spectral slice revealed only 3 "candidate" emission or absorption lines (with $\Delta\chi^2 < -6$). Again, however, the features were seen in only one or two XIS cameras, and Monte Carlo simulations showed that not a single candidate feature was inconsistent with photon noise at greater than 80% confidence. Analysis of the high-and low-flux spectra similarly yielded no significant narrow emission or absorption lines (even at 6.70 and 6.96 keV). Typical upper limits to the eV of an emission line at 5.57 keV (one of the energies of the transient lines in Turner et al. 2002), were $\lesssim$10–15 eV in the time-averaged spectrum or any of the sub-spectra.

7. Discussion

During the late 1990's, NGC 3516 typically displayed a 2–10 keV flux of $\sim$4–6 $\times$ 10^{-11} erg cm^{-2} s^{-1} (e.g., Markowitz, Edelson 2004). During the 2001 *XMM-Newton*/*Chandra* observations, however, the observed 2–10 keV flux was much lower: 1.6–2.3 $\times$ 10^{-11} erg cm^{-2} s^{-1} (Turner et al. 2005). Table 4 lists the inferred absorption-corrected 2–10 keV nuclear fluxes from the *XMM-Newton* observations, as well as during the 2005 *Suzaku* observation. The *Suzaku* observation apparently caught the source in a similar low level of nuclear flux as the 2001 observations. The observed 0.5–2.0 keV flux during the *Suzaku* observation, however, was $\sim$2–3 times lower than during the *XMM-Newton* observations, indicating that the source was still heavily obscured, and confirming that the complex absorption in this source cannot be ignored when fitting the broadband spectrum and modeling diskline components.

7.1. Power-law Components

The primary power-law observed in the hard X-rays is likely emission from a hot corona very close to the supermassive black hole, as seen in all Seyferts. The nature of the soft power-law component, however, is not as clear. It could represent nuclear emission scattered off optically-thin material (e.g., in the optical Narrow Line Region). The normalization of the soft power-law relative to that of primary power-law is 4.2$\pm$0.4%, indicating a column density for the scattering material of roughly 5×10^{22} cm^{-2} (assuming a covering fraction of unity), consistent with this notion. Using *Chandra*-ACIS, George et al. (2002) found the extended circumnuclear gas to have a 0.4–2.0 keV flux of roughly 10$-$14 erg cm^{-2} s^{-1}. However, that emission was studied over an annular extraction region 3″ to 10″; this flux value is likely a lower limit to

the 0.4–2.0 keV flux that the XIS has observed, and so we cannot rule out the hypothesis that the soft power-law component is scattered emission. Alternatively, the soft power-law could be unobscured, "leaked" nuclear emission as part of a partial covering scenario. In this case, the primary absorber would obscure 96% of the sky as seen from the nuclear continuum source. The very low level of 0.3–1.0 keV variability observed could argue for the soft power-law to originate in scattered emission, since we might expect to observed variability of the same amplitude as the 2–10 keV band only if the soft power-law were leaked nuclear emission. However, this is far from certain, as the presence of the soft emission lines in the XIS spectrum could contribute to dilution of the observed variability of the soft power-law. A broadband observation spanning a larger observed flux range is needed to clarify this issue. The soft power-law could of course represent a blend of scattered emission plus leaked nuclear emission. We therefore conclude that primary absorber has a covering fraction between 96–100%.

7.2. Complex absorption

We detect two zones of absorption: the primary absorber, with a covering fraction of 96–100%, and the high-ionization absorber, assumed here to have a covering fraction of unity. The high-ionization absorber is likely the same as that reported by Turner et al. (2005); we find a column density $N_{\rm H}$ of $4.0^{+4.6}_{-3.1}$ $\times 10^{22}$ cm^{-2}, consistent with the column density of 2×10^{22} cm^{-2} used by Turner et al. (2005). Previous studies of NGC 3516, such as Netzer et al. (2002), have discussed in detail the UV absorber, responsible for H Lyα, C IV and N V absorption features in *Hubble Space Telescope* spectra (Kraemer et al. 2002). In the X-ray band, discrete features associated with Mg VII–IX and Si VII–IX are expected from this component, but with the CCD resolution and the calibration-related artifacts near 1.7–1.8 keV in the XIS, such features would likely not be detected by *Suzaku*.

Suzaku has found the primary absorber of the hard X-ray continuum to be lowly-ionized ($\log(\xi) = 0.3\pm0.1$ erg cm s^{-1}), with a column density $N_{\rm H}$ of 5.5 ± 0.2 $\times 10^{22}$ cm^{-2}. It is possible that it is the same absorber that Turner et al. (2005) designated as the "heavy" partial-covering absorber. In this case, the column density has decreased by a factor of 4.5 over a four year timescale, while the covering fraction has increased from ~40–60% to 96–100%. However, because we have not actually observed a specific blob of absorbing gas moving into or out of the line of sight, it is not clear whether the covering fractions derived are associated with single, large blobs partially blocking the line of sight to the X-ray continuum source, or if the absorber consists of numerous, discrete blobs. On the other hand, given the four year gap between the *XMM-Newton* and *Suzaku* observations, it is certainly plausible that the 2001 and 2005 observations could have caught two independent, discrete blobs with differing column densities and differing physical sizes and/or radial distances lying on the line of sight.

To estimate the distance r between the central black hole and the absorbing gas, we can use $\xi = L_{2-200}/(n\ r^2)$, where n is the number density. L_{2-200} is the 2–200 keV illuminating

continuum luminosity, and ξ is measured to be 2 erg cm s^{-1}. We estimate the maximum possible distance to the material by assuming that the thickness Δr must be less than the distance r. The column density $N_{\rm H} = n\Delta r$, yielding the upper limit $r < L_{2-200}/(N_{\rm H}\xi)$. We estimate the 2–200 keV flux from the baseline model to be 1.47×10^{-10} erg cm^{-2} s^{-1}, which corresponds to $L_{2-200} = 2.6 \times 10^{43}$ erg s^{-1} (assuming $H_{\rm o} = 70$ km s^{-1} Mpc^{-1} and $\Lambda_{\rm o} = 0.73$). r is thus <2 $\times10^{20}$ cm (250 light-years), a very loose upper limit encompassing both distances associated with the BLR ($\sim$10 light-days; Peterson et al. 2004) and a possible cold molecular torus at a 1 pc radius.

7.3. Fe K emission components and Compton reflection

A consequence of *Suzaku's* broad bandpass is that we have deconvolved the broadband emitting components, and determined that 1) the broad Fe line was robust in that it was required in all models for an adequate fit, and 2) a partial covering component could not mimic the curvature associated with a relativistic broad line. The best-fit disk inclination was typically $\lesssim$25°. The inner radius was typically $\lesssim 5R_{\rm g}$, suggesting that the black hole is not a Kerr black hole, and may be spinning. The line energy was seen to be consistent with neutral to mildly-ionized Fe (up to Fe $\sim$ XX; Kallman et al. 2004).

We measured a narrow Fe Kα line width of 2800^{+1200}_{-1500} km s^{-1} FWHM. We note that this velocity is roughly commensurate with the optical Broad Line Region; Peterson et al. (2004) reported FWHM velocities for the Hα and Hβ lines of 4770$\pm$893 and 3353$\pm$310 km s^{-1}, respectively. The line energy was also consistent with neutral Fe.

It is possible that the same material that absorbs the hard X-rays is responsible for producing the narrow Fe line. The fact that no Compton hump or 6.2 keV Compton shoulder are seen, implying an origin for the Fe Kα line in Compton-thin material, supports this notion. On the other hand, the material cannot have a column substantially less than $10^{\sim22}$ cm^{-2} or else there would be insufficient optical depth to produce a prominent Fe K line. As an estimate of the Fe Kα equivalent width expected in this case, we can assume an origin in optically-thin gas which completely surrounds a single X-ray continuum source and is uniform in column density, and use the following equation:

$$EW_{\rm calc} = f_{\rm c}\omega f_{\rm K\alpha} A \frac{\int_{E_{\rm Kedge}}^{\infty} P(E)\sigma_{\rm ph}(E)N_{\rm H}dE}{P(E_{\rm line})} \quad (1)$$

Emission is assumed to be isotropic. Here, $f_{\rm c}$ is the covering fraction, initially assumed to be 1.0. ω is the fluorescent yield, 0.34 (Kallman et al. 2004). $f_{\rm K\alpha}$ is the fraction of photons that go into the Kα line as opposed to the Kβ line; this is 0.89 for Fe I. A is the number abundance relative to hydrogen. We assumed solar abundances, using Lodders (2003). $P(E)$ is the spectrum of the illuminating continuum at energy E; $E_{\rm line}$ is the Kα emission line energy. $\sigma_{\rm ph}(E)$ is the photo-ionization cross section assuming absorption by K-shell electrons only

(Veigele 1973[3]).

For $N_{\rm H} = 5.5{\times}10^{22}$ cm^{-2}, $EW_{\rm calc} = 29$ eV, substantially lower than the observed EW. We conclude that it is possible for the absorbing material to contribute to the observed EW, but there is also likely contribution from some other (non-continuum absorbing) material, likely with column densities $\gtrsim 10^{23}$ cm^{-2} (e.g., Matt et al. 2002). For instance, if the putative cold molecular torus does not intersect the line of sight, it could contribute to the observed EW. However, the fact that we have resolved the narrow line and obtained a lower limit of 1300 km s^{-1} to the FWHM velocity width could indicate that the torus, where the FWHM velocities would likely be $\lesssim$ 1000 km s^{-1}, does not dominate in its contribution to the narrow line EW.

Finally, we discuss the origin of the material that gives rise to the observed strong Compton reflection hump. The primary absorber lacks the necessary column density, and is excluded. As far as an origin in the same material that yields the broad or narrow Fe lines is concerned, we note that George, Fabian (1991) calculated that R=1 corresponds to an observed line EW of 150 eV for neutral Fe. In our baseline model, we found a best-fit value of R=1.7, which corresponds to a line EW of 255 eV, closer to the observed EW of the broad line (287 eV in the baseline model) than the narrow line (123 eV). This is consistent with the broad line originating in a Compton-thick disk. Combined with the lack of a prominent Compton shoulder, the narrow line is thus consistent with arising in Compton-thin material commensurate with the BLR. If there does exist a molecular torus, it might not be highly Compton-thick or cover a large fraction of the sky as seen from the central black hole, otherwise it would also make a significant contribution to the observed Compton reflection strength.

Suzaku has observed other Seyferts to display reduced levels of variability in the PIN band compared to the 2–10 keV band, e.g., in MCG–6-30-15 (Miniutti et al. 2007). This behavior is thought to be caused by the presence of the relatively non-varying Compton reflection hump, which dilutes the observed >10 keV variability of the power-law component. We would need to observe NGC 3516 over a larger >12 keV X-ray flux range than in the *Suzaku* observation to potentially observe any significant variability in the PIN band.

8. Summary of Main Results

We have reported on a 150 ksec observation of NGC 3516 made with the *Suzaku* observatory in October 2005. The good exposure times after screening were 135 ks for the XIS cameras and 106 ks for the HXD-PIN.

Our best-fit broadband model included a primary power-law with photon index Γ=1.912±0.025 in our baseline model, absorbed by a column of material with $N_{\rm H}$ = 5.5±0.2×10^{22} cm^{-2} and with log(ξ)=0.3 erg cm s^{-1}. We also modeled a soft power-law component which could be scattered nuclear emission off optically-thin material, unobscured "leaked"

[3] http://www.pa.uky.edu/~verner/photo.html

nuclear emission, or a blend of both. We conclude that the hard X-ray absorber could be a partial coverer, with a covering fraction 96–100%. If this absorber is the same "heavy" absorption component reported by Turner et al. (2005) in the 2001 *XMM-Newton* observations, then between 2001 and 2005 the column density of this absorber decreased by a factor of 4.5, while the covering fraction increased substantially, leading to an observed 0.5–2.0 keV flux a factor of 2–3 lower in 2005 than in 2001. We also modeled a highly-ionized absorber with a column density $N_{\rm H}$ of $4.0^{+4.6}_{-3.1} \times 10^{22}$ cm^{-2}, ionization parameter $\log(\xi) = 3.7^{+0.3}_{-0.7}$ erg cm s^{-1}, and assumed to have a covering fraction of unity.

Our baseline model also included a dozen narrow emission lines originating in He-like N, O, Ne and Mg, H-like C, N, O, Ne and Mg and at least three RRC lines, consistent with an origin in photo-ionized material. However, we cannot exclude a contribution from collisionally-ionized material, as suggested by the presence of an Fe L line near 0.83 keV.

The broad line has been robustly detected: thanks to *Suzaku*'s broad bandpass, we can distinguish between the curvature in the observed continuum due to a partial coverer and that due to a broad diskline; we conclude that for this observation of NGC 3516, a diskline is preferred and that a partial coverer cannot mimic the curvature of the diskline. The broad and narrow lines are decoupled thanks to the narrow response of the XIS and the subsequent high signal/noise ratio in the narrow line. Given the observed equivalent widths of the broad and narrow Fe lines, the value of $R = 1.7^{+0.4}_{-0.5}$ is more consistent with an origin in the same material that gives rise to the broad line, e.g., the accretion disk. The narrow Fe line, meanwhile, has a FWHM velocity width of 2800^{+1200}_{-1500} km s^{-1}, indicating an origin in material with the same velocity as NGC 3516's BLR.

The authors gratefully acknowledge the dedication and hard work of the *Suzaku* hardware teams and operations staff for making this observation possible and for assistance with data calibration and analysis. This research has made use of HEASARC online services, supported by NASA/GSFC. This research has also made use of the NASA/IPAC Extragalactic Database, operated by JPL/California Institute of Technology, under contract with NASA.

References

Blustin, A.J., Page, M.J., Fuerst, S.V., Branduardi-Raymont, G., Ashton, C.E. 2005, A&A, 431, 111

Crenshaw, D.M., Maran, S.P., Mushotzky, R.F. 1998, ApJ, 496, 797

Dickey, J., Lockman, F. 1990, ARAA, 28, 215

Fabian, A.C. et al. 2002, MNRAS, 335, L1

Frontera, F. et al. 2007, ApJ, in press (astro-ph/0611228)

Fujimoto, R. et al. 2007, PASJ, 59S, 113

George, I.M. et al. 2002, ApJ, 571, 265

George, I.M. Fabian, A.C. 1991, MNRAS, 249, 352

Gruber, D.E., Matteson, J.L., Peterson, L.E., Jung, G.V. 1999, ApJ, 520, 124

Haardt, F., Maraschi, L., Ghisellini, G. 1994, ApJL, 432, L95

Ishisaki, Y. et al. 2007, PASJ, 59S, 113

Kallman, T.R., Palmeri, P., Bautista, M.A., Mendoza, C., Krolik, J.H. 2004, ApJS, 155, 675

Keel, W.C. 1996, AJ, 111, 696

Kolman, M., Halpern, J.P., Martin, C., Awaki, H., Koyama, K. 1993, ApJ, 403, 592

Kokubun, M. et al. 2007, PASJ, 59S, 53

Koyama, K. et al. 2007, PASJ, 59S, 23

Kraemer, S.B., Crenshaw, D.M., George, I.M., Netzer, H., Turner, T.J., Gabel, J.R. 2002, ApJ, 577, 113

Lamer, G., Uttley, P., M^{c}Hardy, I.M. 2003, MNRAS, 342, L41

Laor, A. 1991, ApJ, 376, 90

Lodders, K. 2003, ApJ, 591, 1220

Markowitz, A., Reeves, J.N., Braito, V. 2006, ApJ, 646, 783

Mathur, S., Wilkes, B., Aldcroft, T. 1997, ApJ, 478, 182

Matt, G. 2002, MNRAS, 337, 147

Miniutti, G. et al. 2007, PASJ, 59S, 315

Mitsuda, K. et al. 2007, PASJ, 59S, 1

Mizuno, T. et al. 2006, JX-ISAS-SUZAKU-MEMO-2006-42, "Reproducibility of the HXD PIN Non X-ray background"

Nandra, K., Mushotzky, R.F., Yaqoob, T., George, I.M., Turner, T.J. 1997, MNRAS, 284, L7

Netzer, H., Chelouche, D., George, I.M., Turner, T.J., Crenshaw, D.M., Kraemer, S.B., Nandra, K. 2002, ApJ, 571, 256

Peterson, B.M. et al. 2004, ApJ, 613, 682

Porquet, D., Reeves, J.N., Uttley, P., Turner, T.J. 2004, A&A, 427, 101

Pounds, K.A., Nandra, K., Stewart, G.C., George, I.M., Fabian, A.C. 1990, Nature, 344, 132

Puccetti, S., Risaliti, G., Fiore, F., Elvis, M., Nicastro, F., Perola, G.C., Capalbi, M. 2004, Nucl. Phys. B (Proc. Suppl.), 132, 225

Reeves, J.N., Nandra, K., George, I.M., Pounds, K.A., Turner, T.J., Yaqoob, T. 2004, ApJ, 602, 648

Risaliti, G., Elvis, M., Fabbiano, G., Baldi, M., Zezas, A. 2005, ApJ, 623, L93

Risaliti, G., Elvis, M., Nicastro, F. 2002, ApJ, 571, 234

Ross, R.R., Fabian, A.C. 2005, MNRAS, 358 211

Serlemitsos, P. et al. 2007, PASJ, 59S, 9
Shapiro, S., Lightman, A., Eardley, D. 1976, ApJ, 204, 187
Sunyaev, R., Titarchuk, L. 1980, A&A, 86, 121
Takahashi, T. et al. 2007, PASJ, 59S, 35
Tanaka, Y. et al. 1995, Nature, 375, 659
Turner, T.J. et al. 2002, ApJ, 574, L123
Turner, T.J., Kraemer, S.B., Mushotzky, R.F., George, I.M., Gabel, J.R. 2003, ApJ, 594, 128
Turner, T.J., Kraemer, S.B., George, I.M., Reeves, J.N., Bottorff, M.C. 2005, ApJ, 618, 155
Ulrich, M.-H., Boisson, C. 1983, ApJ, 267, 515
Urry, C.M., Padovani, P. 1995, PASP, 107, 803
Vaughan, S., Edelson, R., Warwick, R., Uttley, P. 2003, MNRAS, 345, 1271
Veigele, W.M. 1973, Atomic Data Tables, 5, 51
Yaqoob, T. et al. 2007, PASJ, 59S, 283
Yaqoob, T., Padmanabhan, U. 2004, ApJ, 604, 63

Table 1. Soft X-ray Emission Lines

Line Energy (keV)	Line Identification	Intensity (10^{-6} ph cm^{-2} s-1)	EW (eV)	$-\Delta\chi^2$	F-test Probability
0.366†	C VI	88±26	32±9	22.71	2.1×10^{-5}
0.427†	N VI	42±11	20±5	25.00	7.3×10^{-6}
0.495±0.005	N VII/C VI RRC blend	34±7	22±5	47.34	2.2×10^{-10}
0.563±0.004	O VII	77±10	63±8	154.92	2.9×10^{-31}
$0.665^{+0.012}_{-0.008}$	O VIII	15±4	16±4	30.04	6.9×10^{-7}
0.739†	O VII RRC	6.3±2.9	8.6±4.0	12.62	5.4×10^{-4}
0.830±0.017	Fe L XVII	$6.2^{+7.8}_{-2.7}$	$8.4^{+10.6}_{-3.7}$	14.36	1.1×10^{-3}
0.871†	O VIII RRC	13^{+5}_{-10}	20^{+8}_{-15}	6.94	1.0×10^{-2}
0.917±0.007	Ne IX	16^{+4}_{-3}	26^{+7}_{-5}	141.41	1.0×10^{-28}
1.020†	Ne X	5.6±1.5	14±4	37.45	2.9×10^{-9}
1.196†	Ne IX RRC	5.2±1.2	18±4	48.22	1.7×10^{-11}
1.351±+0.006	Mg XI	$6.9^{+0.9}_{-1.3}$	30^{+4}_{-6}	103.62	1.8×10^{-21}
1.471†	Mg XII	2.8±1.0	14±5	20.25	1.2×10^{-5}

Results are for our best-fit baseline model.

† denotes a fixed parameter.

Table 2. Best-fit parameters for the 1-absorber model and the baseline (2-absorber) model

		1-absorber Model	Baseline (2-absorber) Model
χ^2/dof		1521.46/1419	1485.04/1417
Γ		$1.867^{+0.033}_{-0.042}$	1.904±0.025
Primary Power-law Norm.[1]		$8.8^{+0.4}_{-0.2} \times 10^{-3}$	9.5±0.5 $\times 10^{-3}$
Primary absorber	$N_{\rm H}$ (10^{22} cm^{-2})	5.5±0.2	5.5±0.2
	log(ξ) (erg cm s^{-1})	0.3±0.1	0.3±0.1
Soft Power-law Norm.[1]		3.9±0.2 $\times 10^{-4}$	4.0±0.2 $\times 10^{-4}$
High-ionization absorber	$N_{\rm H}$ (10^{22} cm^{-2})	–	$4.0^{+4.6}_{-3.1}$
	log(ξ) (erg cm s^{-1})	–	$3.7^{+0.3}_{-0.7}$
Fe Kα diskline	Energy (keV)	$6.40^{+0.18}_{-0.00}$	$6.48^{+0.13}_{-0.08}$
	$R_{\rm in}$ ($R_{\rm g}$)	<3.5	<3.5
	Inclination i	<23°	25^{+7}_{-8}°
	Intensity (ph cm^{-2} s^{-1})	$1.33^{+0.21}_{-0.16} \times 10^{-4}$	$1.22^{+0.21}_{-0.10} \times 10^{-4}$
	EW (eV)	296^{+47}_{-36}	287^{+49}_{-24}
Narrow Fe Kα line	Intensity (ph cm^{-2} s^{-1})	5.3±0.4×10^{-5}	5.2±0.3×10^{-5}
	EW (eV)	132±10	123±7
Compton reflection strength R		$1.4^{+0.22}_{-0.3}$	$1.7^{+0.4}_{-0.5}$

[1]Units of power-law normalization are ph keV^{-1} cm^{-2} s^{-1} keV^{-1} at 1 keV.

[2] PEXRAV inclination angle set at 20°.

Table 3. Best-fit parameters for models with partial covering components

		Model PC1	Model PC2	Model PC3
χ^2/dof		1485.69/1416	1480.48/1414	1676.57/1418
Γ		$1.931^{+0.027}_{-0.057}$	$1.972^{+0.011}_{-0.036}$	$2.051^{+0.046}_{-0.048}$
Primary Power-law Norm.[1]		$7.5\pm0.2\times10^{-3}$	$9.8^{+0.3}_{-0.7}\times10^{-3}$	$1.3^{+0.1}_{-0.2}\times10^{-2}$
Primary absorber	$N_{\rm H}$ (10^{22} cm^{-2})	5.5 ± 0.1	$6.1^{+0.2}_{-0.1}$	5.3 ± 0.2
	log(ξ) (erg cm s^{-1})	0.3 ± 0.1	0.3 ± 0.1	$0.1^{+0.2}_{-0.1}$
Partial covering Component	$N_{\rm H}$ (10^{22} cm^{-2})	5.5[2]	$1.0^{+1.3}_{-0.2}$	$7.8^{+68}_{-3.8*}$
	log(ξ) (erg cm s^{-1})	0.3[2]	$-1.3^{+0.5}_{-1.7*}$	$-0.3^{+0.8}_{-2.7*}$
	Power-law Norm.[1]	$2.4\pm0.2\times10^{-3}$	$8.8^{+3.9}_{-2.3}\times10^{-4}$	$<2.4\times10^{-3}$
Soft Power-law Norm.[1]		$4.0\pm0.1\times10^{-4}$	$3.7^{+0.2}_{-0.3}\times10^{-4}$	$4.1^{+0.1}_{-0.3}\times10^{-4}$
High-ionization absorber	$N_{\rm H}$ (10^{22} cm^{-2})	4.1 ± 2.5	$3.3^{+1.8}_{-1.3}$	$11.7^{+2.8}_{-0.4}$
	log(ξ) (erg cm s^{-1})	$3.3^{+0.3}_{-0.1}$	$3.5^{+0.8}_{-0.2}$	3.2 ± 0.1
Fe Kα diskline	Energy (keV)	$6.45^{+0.15}_{-0.05*}$	$6.45^{+0.10}_{-0.05}$	–
	$R_{\rm in}$ ($R_{\rm g}$)	<3.2	<4.3	–
	Inclination i	$26^{+4\circ}_{-6}$	$26^{+4\circ}_{-8}$	–
	Intensity (ph cm^{-2} s^{-1})	$1.18^{+0.25}_{-0.17}\times10^{-4}$	$1.13^{+0.25}_{-0.15}\times10^{-4}$	–
	EW (eV)	268^{+57}_{-39}	266^{+56}_{-34}	–
Narrow Fe Kα line	Intensity (ph cm^{-2} s^{-1})	$5.4^{+0.5}_{-0.4}\times10^{-5}$	$5.4^{+0.5}_{-0.4}\times10^{-5}$	$8.8\pm0.7\times10^{-5}$
	EW (eV)	153^{+14}_{-11}	134^{+12}_{-10}	226 ± 18
Compton reflection strength R		$1.7^{+0.2}_{-0.4}$	$1.8^{+0.4}_{-0.5}$	$2.4^{+0.93}_{-0.3}$

An asterisk (*) denotes that the parameter uncertainty pegged at the hard limit.

[1] Units of power-law normalization are ph keV^{-1} cm^{-2} s^{-1} keV^{-1} at 1 keV.

[2] parameters tied to those of the primary absorber.

[3] PEXRAV inclination angle set at 25°.

Table 4. Comparison to the 2001 *XMM-Newton* observations

	Suzaku Oct. 2005	*XMM-Newton* Apr. 2001	*XMM-Newton* Nov. 2001
Absorption-corrected 2–10 keV flux (erg cm^{-2} s^{-1})	3.4×10^{-11}	2.7×10^{-11}	1.9×10^{-11}
Observed 0.5–2.0 keV flux (erg cm^{-2} s^{-1})	1.3×10^{-12}	4.3×10^{-12}	2.9×10^{-12}
Primary absorber $N_{\rm H}$ (10^{22} cm^{-2})	5.5 ± 0.2	25 ± 1	25 ± 1
Primary absorber covering fraction	96–100%	44 ± 6%	58 ± 5%
High-ionization $N_{\rm H}$ (10^{22} cm^{-2})	$4.0^{+4.6}_{-3.1}$	1.6†	1.6†

Results for the *XMM-Newton* spectra were taken from Turner et al. (2005).

Results for *Suzaku* are from the best-fit baseline model.

† denotes a fixed parameter.

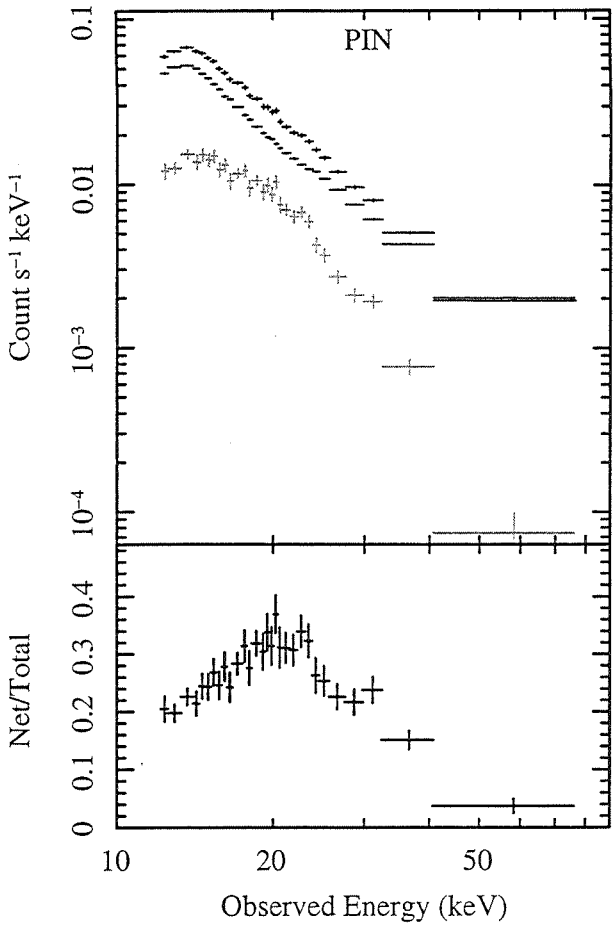

Fig. 1. HXD-PIN spectrum. The upper panel shows the net source spectrum (*gray points*), the background (*lower black points*), and the total (source + background) spectrum (*upper black points*). The PIN spectra have been binned such that the net spectrum has a minimum signal-to-noise ratio of 8σ per bin. The lower panel shows the ratio of the net source spectrum to the total spectrum.

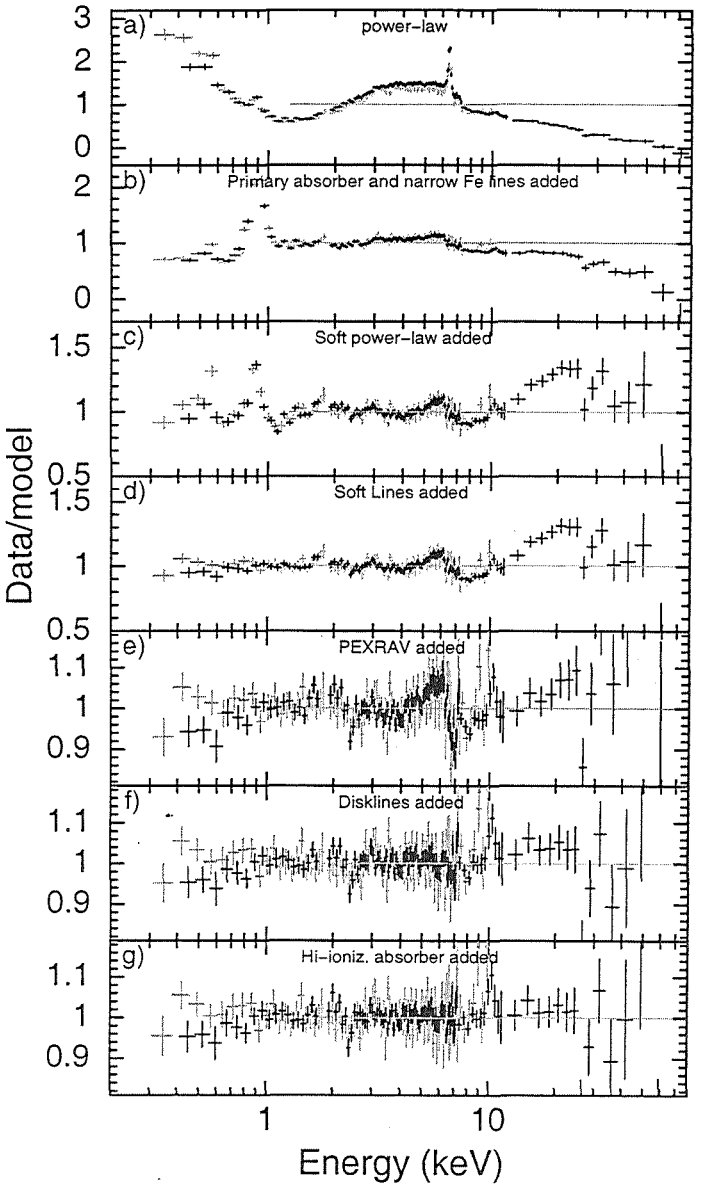

Fig. 2. Data/model residuals for selected broadband models. Panel a) shows residuals to a simple power-law. Panel b) shows the residuals after the primary absorber and narrow Fe lines are included in the model. Panel c) shows residuals after the soft power-law is included. In panel d), the soft emission lines have been modeled. In panel e), a PEXRAV reflection component has been added. In panel f), diskline components have been added. In panel g), the high-ionization absorber has been added to yield our baseline model. Black points <12 keV denote the (co-added) XIS-FI spectrum. Gray points denote the BIS-BI spectrum. Black points >12 keV denote the PIN data. Rest-frame energies are shown. All data have been rebinned with a binning factor of 5, though XIS data >7.2 keV have been rebinned by a factor of 25 for clarity.

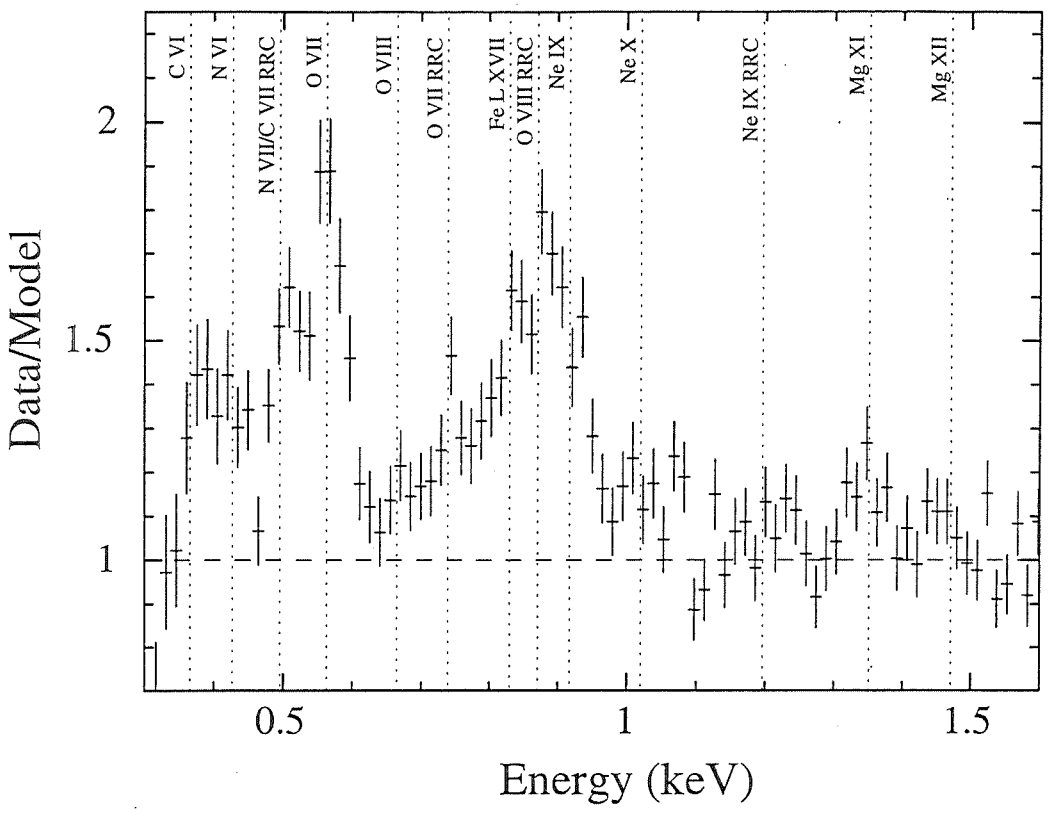

Fig. 3. Ratio of the soft band data to a simple power-law, showing the prominent emission lines. For clarity, only the XIS BI spectrum is shown. Rest-frame energies are shown.

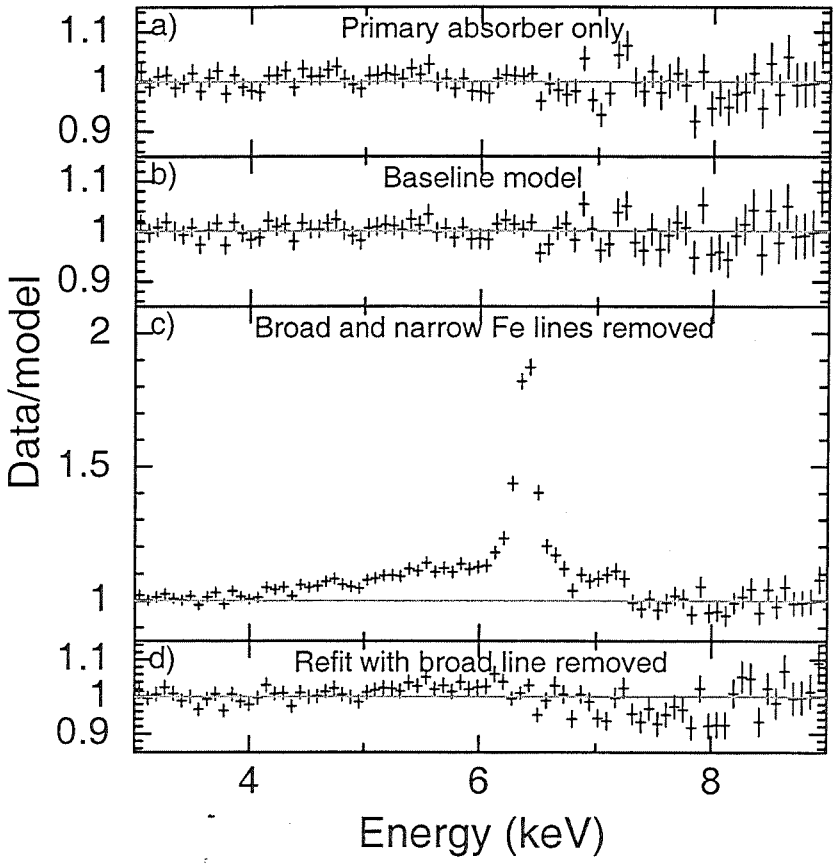

Fig. 4. Data/model residuals to various models are shown, focusing on the Fe K bandpass. Panel a) shows the residuals when the primary absorber is the only zone of absorption modeled. Panel b) shows the residuals to the baseline model, with two zones of absorption; note that residuals near 6.9 keV are now improved. In panel c), the broad and narrow Fe lines have been removed from the baseline model. Panel d) illustrates that when the broad lines are removed from the baseline model and the model is re-fit, large data/model residuals appear in the Fe K bandpass.

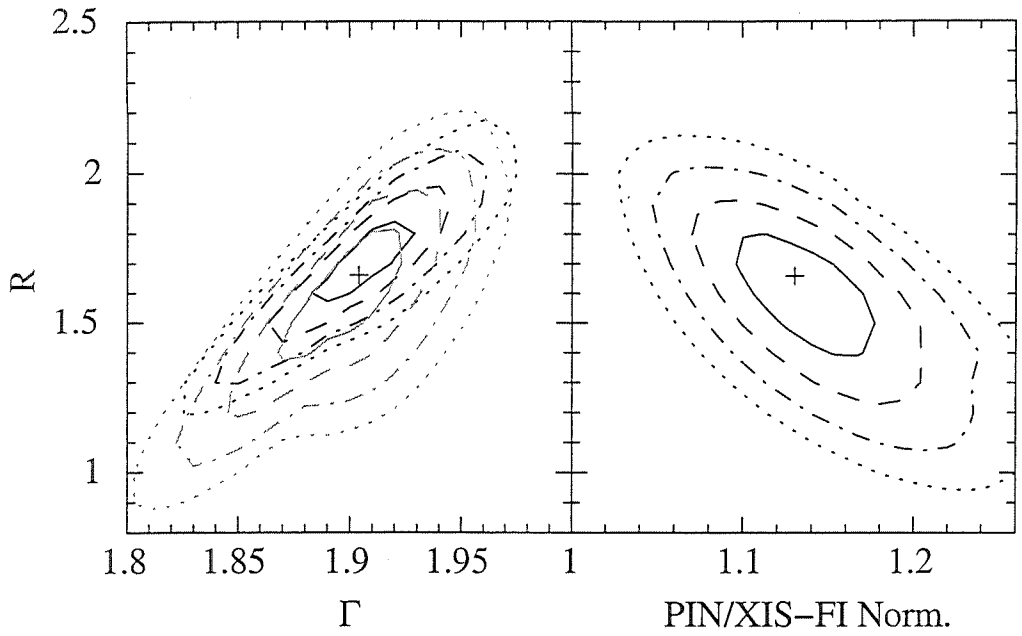

Fig. 5. *Left:* Contour plot of the Compton reflection fraction R versus the photon index of the primary power-law. The black contours show results when the PIN/XIS-FI normalization was kept fixed at 1.13. The gray contours show results when the PIN/XIS-FI normalization was left free. *Right:* Contour plot of R versus the PIN/XIS-FI normalization; Γ was a free parameter. In both plots, dotted, dot-dashed, dashed, and solid lines denote 68, 95.4, 99.73%, and 99.99% confidence levels, respectively.

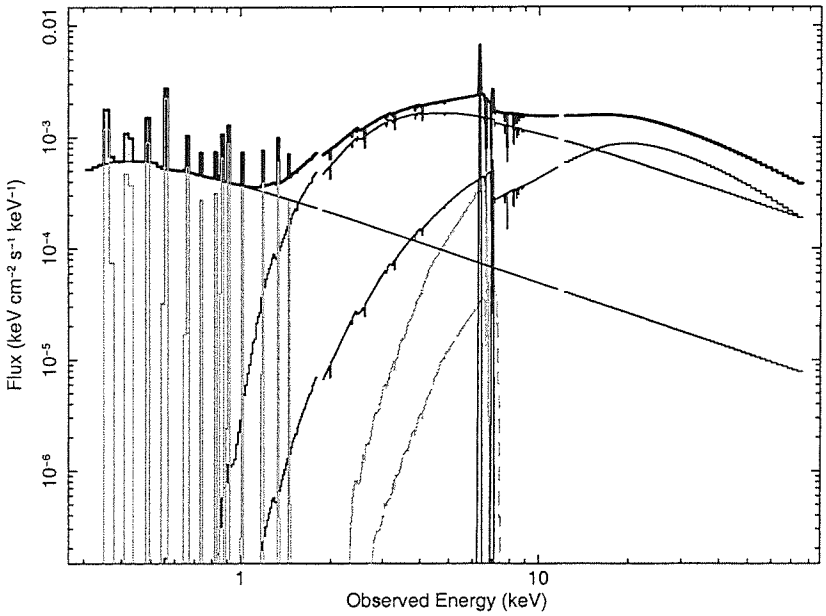

Fig. 6. Unfolded broadband spectrum for the baseline model. The thick black line is the total spectrum. Thin black lines denote the primary, absorbed power-law, the soft power-law, and the reflection component peaking at 20 keV. Gray dashed lines denote the narrow Fe lines. Gray solid lines in the Fe K bandpass are the diskline components. gray solid lines in the soft band denote the soft emission lines.

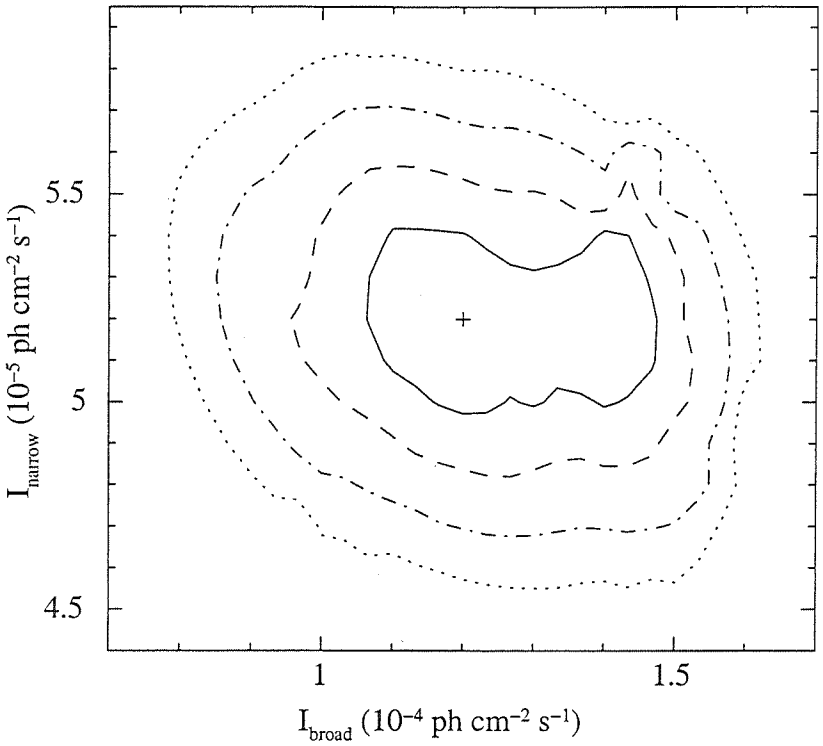

Fig. 7. Contour plot showing the intensity of the narrow Kα line versus that of the broad Kα line. 68, 95.4, 99.73 and 99.994% confidence levels are plotted. Note that the contour plots do not hit 0 demonstrating that the lines are decoupled at the 4σ level.

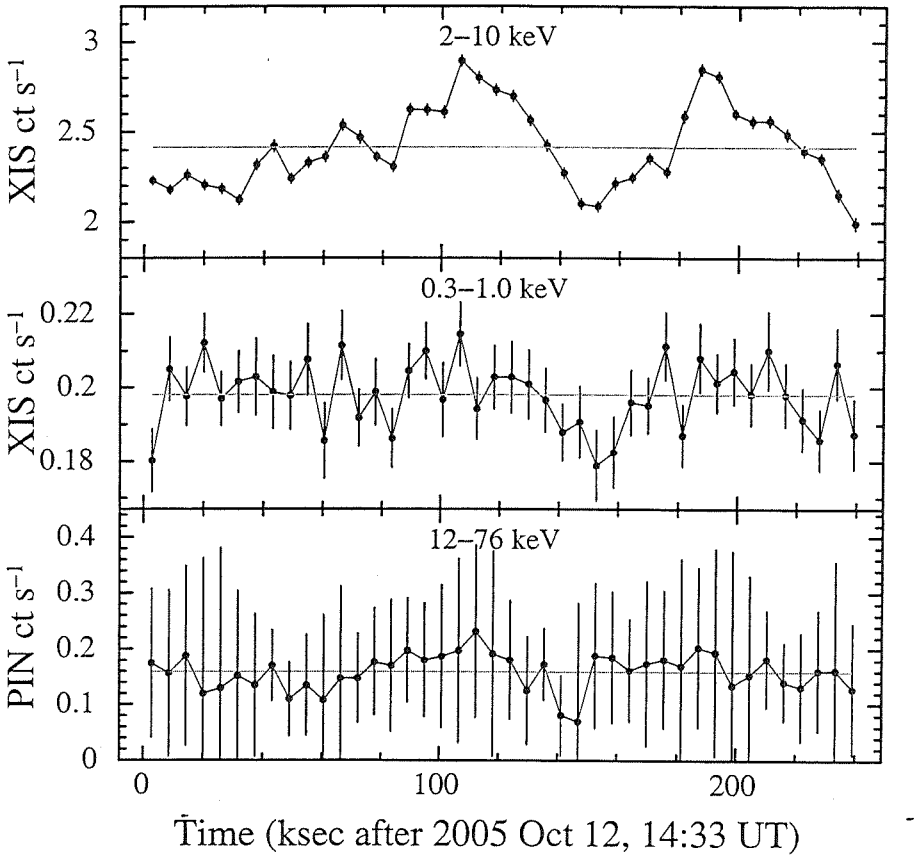

Fig. 8. Orbitally binned XIS and HXD light curves. The top and middle panels respectively show the 2–10 keV and 0.3–1.0 keV count rate light curves, summed over all four XIS cameras and background subtracted. The bottom panel shows the 12–76 keV PIN light curve, also orbitally-binned and background-subtracted. The error bars show only the statistical error of the count rates; systematic uncertaintly associated with subtraction of the non-X-ray background in the PIN is roughly 0.3 ct s^{-1}. The mean count rates are 2.41 ct s^{-1} for 2–10 keV, 0.20 ct s^{-1} for 0.3–1.0 keV, and 0.16 ct s^{-1} for 12–76 keV.